



OPEN

Repair of critical-sized bone defects in rabbit femurs using graphitic carbon nitride (g-C₃N₄) and graphene oxide (GO) nanomaterials

Ahmed Abdelrahiem Sadek¹, Mahmoud Abd-Elkareem², Hani Nasser Abdelhamid^{3,4,5}, Samia Moustafa¹ & Kamal Hussein¹✉

Various biomaterials have been evaluated to enhance bone formation in critical-sized bone defects; however, the ideal scaffold is still missing. The objective of this study was to investigate the in vitro and in vivo regenerative capacity of graphitic carbon nitride (g-C₃N₄) and graphene oxide (GO) nanomaterials to stimulate critical-sized bone defect regeneration. The in vitro cytotoxicity and hemocompatibility of g-C₃N₄ and GO were evaluated, and their potential to induce the in vitro osteogenesis of human fetal osteoblast (hFOB) cells was assessed using qPCR. Then, bone defect in femoral condyles was created in rabbits and left empty as control or filled with either g-C₃N₄ or GO. The osteogenesis of the different implanted scaffolds was evaluated after 4, 8, and 12 weeks of surgery using X-ray, computed tomography (CT), macro/microscopic examinations, and qPCR analysis of osteocalcin (OC) and osteopontin (OP) expressions. Both materials displayed good cell viability and hemocompatibility with enhanced collagen type-I (Col-I), OC, and OP expressions of the hFOB cells. Compared to the control group, the bone healing process in g-C₃N₄ and GO groups was promoted in vivo. Moreover, complete healing of the bone defect was observed radiologically and grossly in g-C₃N₄ implanted group. Additionally, g-C₃N₄ implanted group showed higher percentages of osteoid tissue, mature collagen, biodegradation, and expressions of OC and OP. In conclusion, our results revealed that g-C₃N₄ and GO nanomaterials could induce osteogenesis in critical-sized bone defects.

Critical-sized bone defects have been reported in millions of patients each year due to massive bone loss associated with violent trauma, blast injuries, excision of bone tumors, and skeletal malformations^{1,2}. Although the intrinsic bone healing capacity, bone defect regeneration is impaired when the gap of bone loss exceeds the critical size. Therefore, critical-sized bone defect repair is considered a significant obstacle in orthopedics and represents an important health issue with economic implications³.

Autogenous and allogenic bone implantation has been utilized widely to reconstruct the critical-sized bone defects; however, their clinical application has several restrictions. Autogenous bone implantation is usually associated with limited supply, post-operative pain, blood loss, morbidity of the donor site, and prolonged period of operation. Allogenic bone grafts are vulnerable to the risk of disease transmission, poor osseointegration, and rejection³⁻⁵. These hurdles inspired the development of innovative alternative therapies based on tissue engineering to stimulate and support bone formation^{2,6}. Bone tissue engineering includes a combination of implanted cells, cytokines, and/or biodegradable scaffolds. Scaffolds have an integral role in bone regeneration

¹Department of Surgery, Anesthesiology and Radiology, Faculty of Veterinary Medicine, Assiut University, Assiut 71526, Egypt. ²Department of Cell and Tissues, Faculty of Veterinary Medicine, Assiut University, Assiut, Egypt. ³Advanced Multifunctional Materials Laboratory, Department of Chemistry, Faculty of Science, Assiut University, Assiut, Egypt. ⁴Proteomics Laboratory for Clinical Research and Materials Science, Department of Chemistry, Faculty of Science, Assiut University, Assiut, Egypt. ⁵Nanotechnology Research Centre (NTRC), The British University in Egypt (BUE), Suez Desert Road, El-Sherouk City 11837, Cairo, Egypt. ✉email: kamalhussein@aun.edu.eg; kamalhussein1986@gmail.com

as they provide an extracellular microenvironment that supports cell proliferation and differentiation. Besides, the properties of the ideal scaffolds include excellent biocompatibility, biodegradability, porosity, and mechanical strength^{6–10}.

Different biomaterials have been studied over the last years as a scaffold for bone tissue engineering to repair the critical-sized bone defects; however, none of them is considered ideal^{3–7,11}. Among different biomaterials, carbonaceous nanomaterials (CNs) have been used increasingly in various biomedical applications in the last years¹².

Graphitic carbon nitride (g-C₃N₄) is a CNs with unique optical and electronic properties, low-cost, straightforward synthesis procedures, physicochemical stability, excellent biocompatibility and biometabolizability, and novel fluorescent characteristics¹³. The g-C₃N₄-based nanocomposites have been reported as promising materials for biomedical applications, including tissue regeneration^{14,15}. It has been reported that photoactivated C₃N₄ induces and supports the in vitro osteogenic proliferation and differentiation. In addition, it activates Runt-related transcription factor 2 (Runx2) that promotes the expression of osteoblast marker genes¹⁵.

Graphene oxide (GO) is another CNs that has recently emerged in the biomedical field for scaffold fabrication in tissue engineering^{7,11,16–18}, drug delivery^{19,20}, gene therapy^{21,22}, cancer therapy^{23,24}, wound healing²⁵, and antibacterial^{26,27} as well as antiviral applications^{28,29} due to their unique physicochemical and mechanical properties such as high thermal conductivity³⁰, high drug loading efficiency³¹, and water dispensability³² as well as biocompatibility³³ and biodegradability³⁴. GO and ultrasonicated GO have been reported to provide a favorable platform that enhance and support mesenchymal stem cells (MSCs) adhesion, proliferation, and differentiation into osteogenic lineage cells as well as osteoblast mineralization^{7,11,16,35,36}. Besides, it has been suggested that the hydrophobic π domains in GO structure improve its interactions with proteins through hydrophobic and electrostatic interactions, therefore GO can induce stem cells differentiation into osteogenic cells^{37–39}.

Thus, the main goal of this study is to evaluate the osteo-regenerative efficiency of g-C₃N₄ and GO using in vitro and in vivo studies in a rabbit femoral condyle model. Additionally, it aims to investigate the in vitro and in vivo biocompatibility of g-C₃N₄ and GO scaffolds.

Results

Characterization of g-C₃N₄ and GO nanomaterials.. The synthesis and characterization for g-C₃N₄ and GO nanomaterials are plotted in Fig. 1. As shown in Fig. 1A, the polymerization of melamine at 550 °C resulted in a yellow g-C₃N₄ powder. The XRD pattern of g-C₃N₄ displayed a sharp peak located at $2\theta \approx 27.4^\circ$ with a distance (d) spacing of ~ 0.33 nm, corresponding to the periodic stacking of the conjugated aromatic layers (Fig. 1Ca). TEM imaging of g-C₃N₄ showed a layer stacking of g-C₃N₄ layers⁴⁰ (Fig. 1Cb).

Hummers' method produced a black GO powder (Fig. 1B). XRD pattern of GO showed a diffraction peak at 2θ of 12.0° (d -space = 0.78 nm) and 26.5° (d -space = 0.33 nm) for Miller planes of (001) and (002) for GO and graphite, respectively^{41,42} (Fig. 1Da). TEM imaging of GO showed a transparent particle indicating the formation of a few GO layers (Fig. 1Db). Zeta potential of GO colloidal solution at pH 7 was -45 mV. The high negative zeta potential is due to the oxygen functional groups such as hydroxyl, carbonyl, carboxylate, and epoxide⁴³. The presence of oxygen functional groups enables high dispersion of GO in water. Raman spectrum shows the main characteristic peaks at 1348 cm^{-1} and 1598 cm^{-1} , corresponding to D (vibration of the sp^3 carbon atoms), and G (vibration of the sp^2 carbon atoms), respectively⁴⁴ (Fig. supp 1A). The intensity of I_D/I_G ratio equals 0.96, which is close to the previous value reported for GO (0.97)⁴⁵, indicating multilayer structure. SEM image and elemental analysis using EDS were reported as shown in Fig. supp 1B. The layer morphology of GO can be noticed from

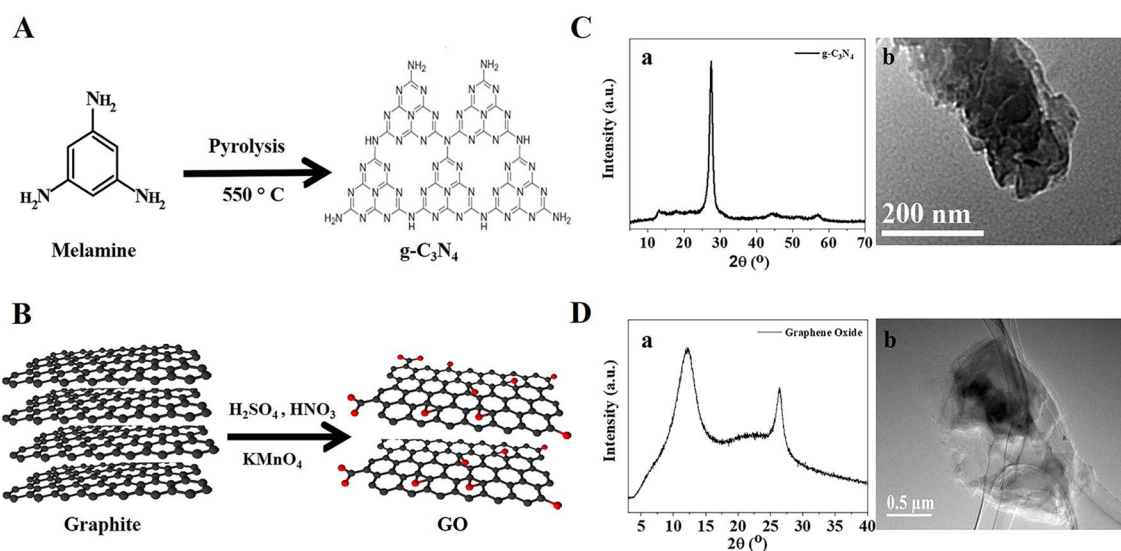


Figure 1. Synthesis and characterization of g-C₃N₄ and GO. (A) Schematic representation for the synthesis of g-C₃N₄ and their characterization (C) using XRD (a), and TEM (b). (B) Schematic representation for the synthesis of GO and their characterization (D) using XRD (a), and TEM (b).

SEM image. EDX analysis shows the presence of 25.4 wt.% oxygen, revealing that the carbon-to-oxygen atomic ratio is 2.8, close to the value reported using Hummer's method^{43,46}.

Indirect contact cytotoxicity assay. The live/dead staining assay revealed that all the preconditioned media from the different nanomaterials revealed only a few positive cells to Ethidium Homodimer-1 staining after 7 days of culture (Fig. 2A).

The proliferation of hFOB cells was evaluated using extraction media prepared from the different samples. On day 1, preconditioned media prepared from both nanomaterials showed viability of more than 95% compared to the negative control by MTT assay ($P < 0.05$) (Fig. 2B). By day 3, preconditioned media prepared from GO nanomaterial revealed higher viability than g-C₃N₄ nanomaterial with percentages of $108.74\% \pm 6.32\%$ compared to $91.7\% \pm 2.87\%$ in g-C₃N₄ ($P < 0.05$). Finally, no significant difference was observed between the different materials on day 7.

Hemocompatibility evaluation. The g-C₃N₄ and GO nanomaterials displayed a non-significant hemolysis rate of $9.64 \pm 4.58\%$ and $7.61 \pm 3.14\%$, respectively, whereas the negative control group (PBS group) had a hemolysis rate of $4.35 \pm 2.58\%$ ($P < 0.05$) (Fig. 2C).

qPCR analysis. The expression of Col-1 in cells cultured on g-C₃N₄ and GO displayed a significantly higher level than the negative control group starting from day 3 till day 28 (Fig. 2D). On day 3 and day 28, no significant difference between the designed nanomaterials was observed. However, Col-1 expression was significantly higher in g-C₃N₄ nanomaterial than in the GO nanomaterial on day 7, day 14, and day 21 with fold changes of 14.34 \pm 2.17-fold, 17.09 \pm 1.5-fold, and 18.73 \pm 2.32-fold, compared to 10.66 \pm 1.11-fold, 12.31 \pm 1.62-fold, and 12.83 \pm 1.22-fold in cells grown on GO, respectively ($P < 0.05$).

OC expression was higher in cells cultured on the designed nanomaterials than in the negative control group (Fig. 2E). On days 7 and 14, hFOB cultured on g-C₃N₄ nanomaterials showed a significantly higher expression than GO nanomaterials ($P < 0.05$). Starting from day 21, the expression of OC decreased gradually till reaching a non-significant level of expression with that in the negative control group at day 28.

Finally, OP expression was significantly higher in the g-C₃N₄ and GO groups at the different evaluation times compared to the negative control group (Fig. 2F). On days 7, 14, 21, and 28, cells on g-C₃N₄ nanomaterial expressed a higher expression of OP (19.25 \pm 2.42, 64.67 \pm 5.98, 47.72 \pm 5.40, and 13.57 \pm 4.70-folds, respectively) compared to GO nanomaterial (12.46 \pm 2.71, 37.64 \pm 5.39, 21.95 \pm 6.48, and 4.92 \pm 2.13-folds, respectively) ($P < 0.05$).

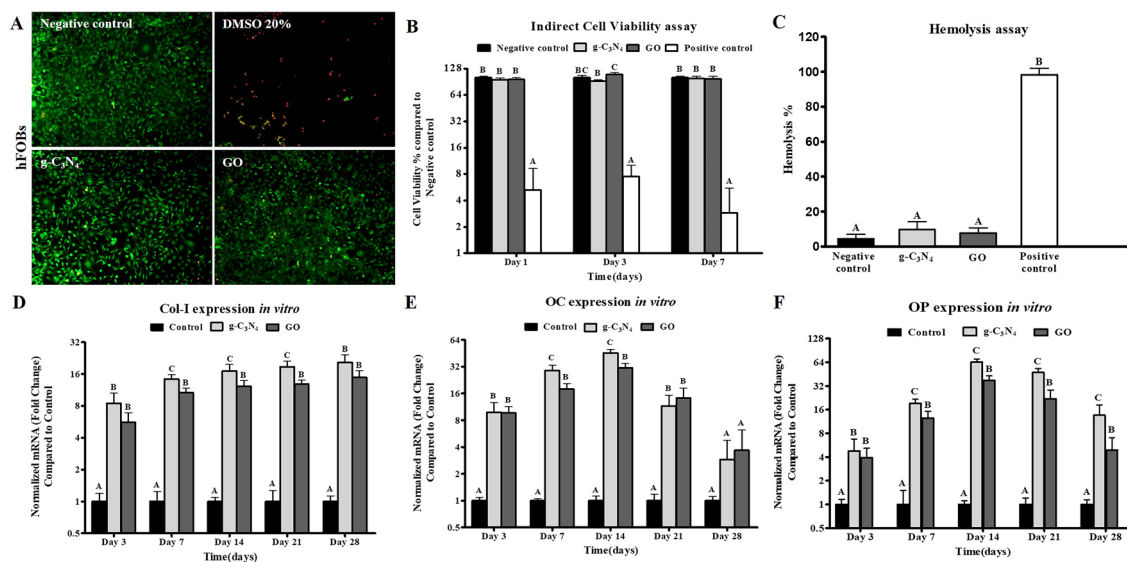


Figure 2. In vitro experiments of g-C₃N₄ and GO. (A) Cell viability using Live/Dead assay for hFOB cells cultured on g-C₃N₄ and GO nanomaterials for 7 days. Live cells were stained green and dead cells were stained red (Scale bar represents 100 μ m, Magnification = 10 \times). (B) MTT cytotoxicity assay for cell viability of hFOB cultured using extracts of g-C₃N₄ and GO nanomaterials for 1, 3 and 7 days compared to the negative control. Error bars represent means \pm standard deviation ($n = 8$). (C) Hemolysis assay using extracts of g-C₃N₄ and GO nanomaterials compared to the negative control. q-PCR analysis for mRNA expression of collagen type 1 (Col-1) (D), osteocalcin (OC) (E), and osteopontin (OP) (F) in negative control cells and on g-C₃N₄ and GO nanomaterials for 28 days, respectively. Error bars represent means \pm SD; $n = 3$ for each group and time point. Bars with the same letter represent not significantly different values (one-way ANOVA followed by Tukey's HSD post hoc test).

Clinical observation. The critical size bone defect was successfully created, as demonstrated in Fig. supp 2. All rabbits survived during and after surgery. They recovered from anesthesia within 30–45 min after surgery and could stand up and move freely within the first 24 h after the operation. They returned to normal activities such as eating, drinking, and grooming within 48 h after surgery. There were neither operative nor postoperative complications such as infection and fracture were recorded. The wound healing was uneventful without dehiscence during the postoperative period for all groups, and the sutures were removed 7–10 days after the surgical operation.

Radiographical assessment. The immediate postoperative radiographs revealed well-defined radiolucent defects in the femoral condyles in different groups of this study (Fig. 3Aa,e,i).

On week 4 after surgery, a well-defined radiolucent defect was already visible in the control group (Fig. 3Ab). However, g-C₃N₄ and GO implanted groups showed increased radiopacity of the bone defects over time (Fig. 3Af,j). The defect sites were more radiopaque than immediate postoperative radiographs in both g-C₃N₄ and GO implanted groups. g-C₃N₄ implanted defects showed new bone formation at the center of these defects with hardly distinct margins, while in GO implanted defects, the new bone formation could be detected within the defects; however, their margins were still clearly distinguishable.

On week 8 after surgery, the control group still displayed a well-demarcated radiolucent defect (Fig. 3Ac). However, in the g-C₃N₄ implanted group, most defects were filled with newly formed bony tissue and markedly indistinct from the surrounding bony tissue (Fig. 3Ag). In addition, in GO implanted group, there was evidence for more bone formation at these defects with hardly distinct margins (Fig. 3Ak).

On week 12 after surgery, the control defects still appeared radiolucent with a small amount of bony tissue formation at their margins (Fig. 3Ad). However, g-C₃N₄ and GO implanted defects were nearly indistinguishable from the adjacent bone and almost as dense as normal bone (Fig. 3Ah,l).

The bone density according to the mean grayscale value per unit area of defects on week 4 after surgery was significantly higher in the g-C₃N₄ implanted group (2861.34 ± 157.9) than in both GO implanted (2218.93 ± 88.2) and control groups (1932.5 ± 226.9) ($P < 0.05$) (Fig. supp 3). However, on week 8 and week 12 after surgery, bone density was significantly higher in both g-C₃N₄ (3203.5 ± 225.02 and 3305.4 ± 160.9, respectively) and GO (2924.7 ± 221.8 and 3259.4 ± 561.9, respectively) implanted groups than the control group (2049.6 ± 63.9 and 2172.5 ± 40.7, respectively) ($P < 0.05$). Furthermore, a non-significant difference was observed between the various implantation time points within the control or g-C₃N₄ implanted groups. In contrast, the GO implanted group displayed a significant difference between week 4 and both weeks 8 and 12 after implantation ($P < 0.05$).

Computed tomography (CT) scanning. No bone union could be detected in the coronal, sagittal, and transverse planes of the control group (Fig. 3Ba–c). However, bone union was detected in g-C₃N₄ and GO implanted defects. The g-C₃N₄ implanted group revealed that the bone defects filled with newly formed bone tissue in the different planes (Fig. 3Be–g), while the GO implanted group showed the presence of islands of newly formed bone within the bone defects (Fig. 3Bi–k).

The results of the different planes were correlated to lateral 3D-CT images (Fig. 3Bd,h,l) whereas bone defects appeared undistinguished with smooth cancellous bone union in g-C₃N₄ implanted group, and were less detectable in GO implanted group.

Gross examination of the bone defects. As shown in Fig. supp 4, the margins of the defects at different evaluation periods were demarcated in the control group. On week 4 after surgery, the g-C₃N₄ implanted group revealed less distinguishable defects margins, while GO implanted group showed a well-defined defects margin. However, the defects' margins were indistinguishable in the g-C₃N₄ implanted group and less demarcated in the GO implanted group at week 8. The margins of the defects in the g-C₃N₄ implanted group at week 12 were indistinguishable, whereas GO implanted group still showed a less detectable defects margin.

The defects in the control group were filled with blood clots and/or connective tissue on week 4 and connective or fatty tissues on weeks 8 and 12 postoperatively.

The g-C₃N₄ implanted defects at week 4 were covered with the yellow particles of the g-C₃N₄ scaffold. In addition, the g-C₃N₄ material was well integrated within the bone defects and appeared binding to the host bone with indistinguishable interface between the scaffolds and host bone. However, bridging bone-like tissue connecting the rims of the bone defects with a little g-C₃N₄ material was observed on week 8. On week 12, bone defects were undistinguished with a smooth surface and a color resembling the surrounding tissue, indicating complete repair of the bone defects in the g-C₃N₄ implanted group with bridging bone-like tissue.

In GO implanted group, the defects at week 4 were covered with the black GO scaffold that was well integrated within the bone defects and appeared bound to the host bone with indistinguishable interface between the GO scaffold and host bone. However, on weeks 8 and 12, bone defects were still covered with the black-colored GO, and partial repair of the bone defects with a bridging smooth bone-like tissue connecting the rims of the bone defects was detected.

Histological examination. Histological evaluation of femoral condyle bone defects harvested on weeks 4, 8, and 12 after surgery was conducted to examine the effect of g-C₃N₄ and GO nanomaterials on bone repair. At week 4, the control bone defects were filled with fatty bone marrow containing abundant fat cells and a few hematopoietic stem cells and MSCs (Fig. 4A,B). However, the bone defect in the g-C₃N₄-implanted group was filled with disintegrated scaffold material separated by osteoid tissue, osteogenic cells, osteoblasts, osteoclasts, and collagen fibers and surrounded by spongy bone trabeculae (Fig. 4C,D). The direction of osteoregeneration was centrifugal. The peripheral zone of the bone defect displayed newly formed woven bone and some MSCs

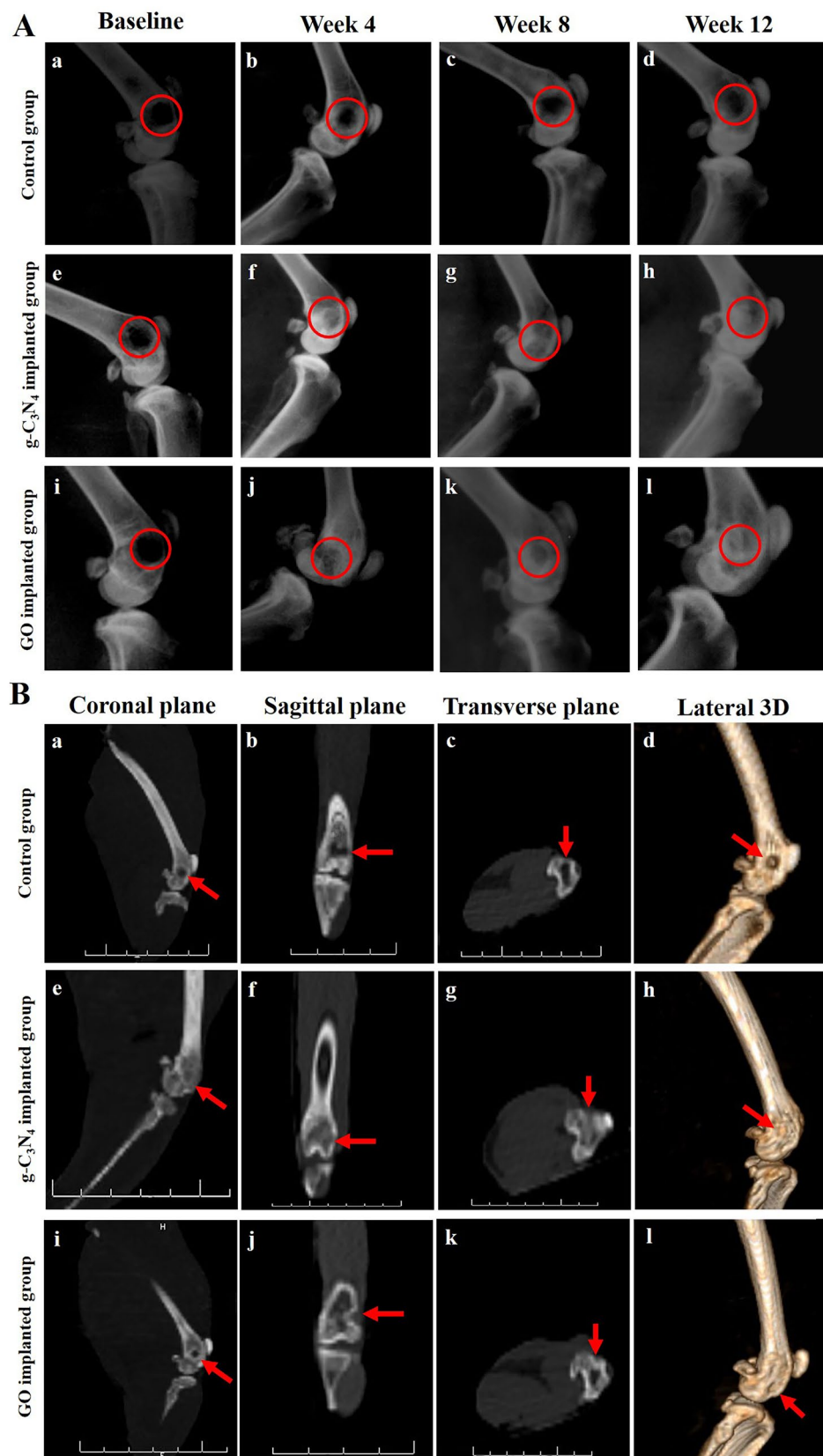


Figure 3. Radiological evaluation of bone repair. **(A)** Lateromedial radiographs of the defect site of control (a–d), g-C₃N₄ implanted (e–h), and GO implanted (i–l) groups at different post-implantation times. **(B)** CT scanning of defect site of control (a–d), g-C₃N₄ implanted (e–h), and GO implanted (i–l) groups at week 12 after surgery.

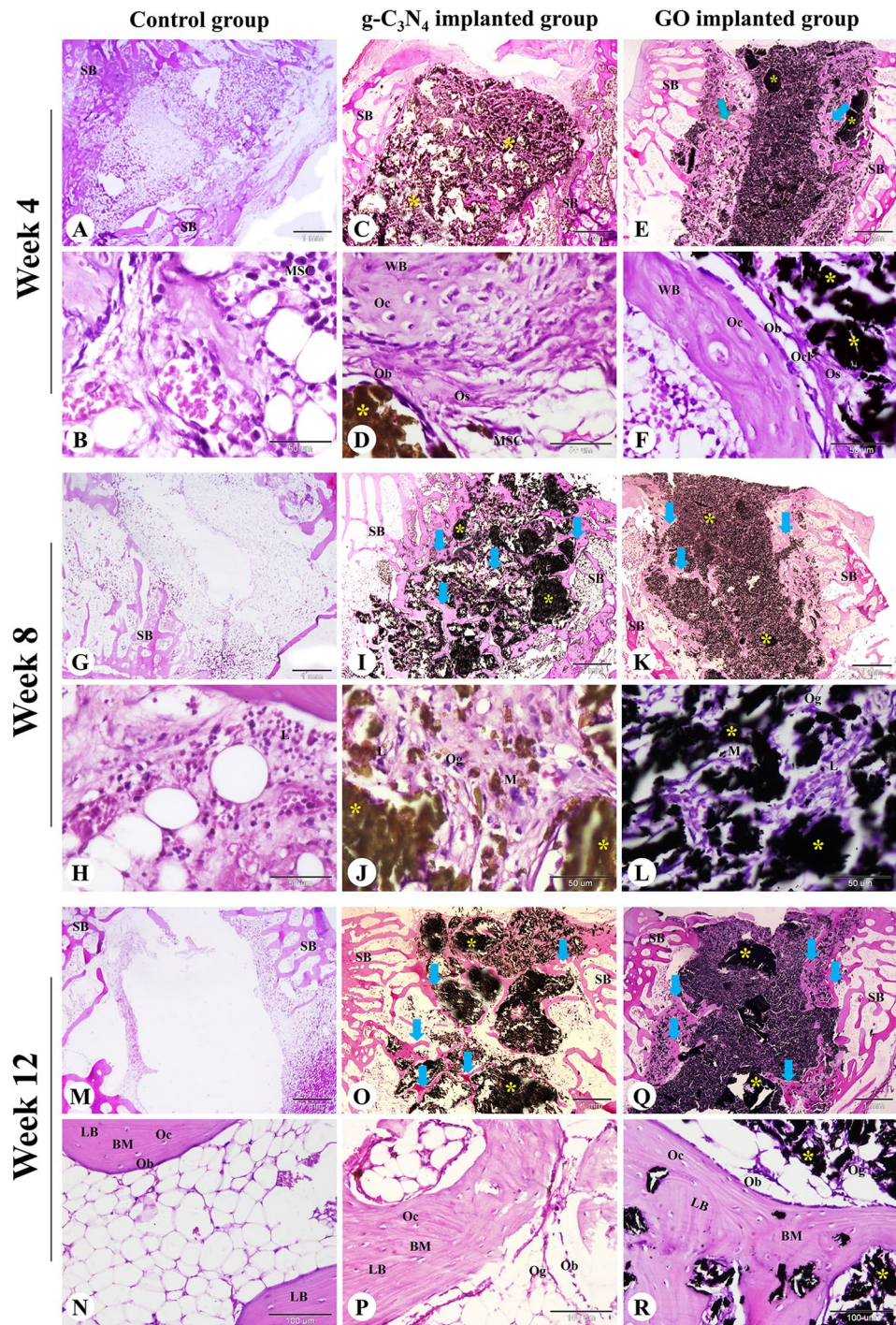


Figure 4. Histological evaluation of femoral condyle defects in rabbits. The repair site of the femoral condyle at week 4 (A–F), 8 (G–L), and 12 (M–R) after surgery in control, g-C₃N₄ implanted, and GO implanted groups was stained with H&E. SB spongy bone, MSC mesenchymal stem cell, Ob osteoblast, Oc osteocyte, Ocl osteoclast, Og osteogenic cells, Os osteoid tissue, BM bone matrix, WB woven bone, LB lamellar bone, L lymphocyte, M macrophage; yellow asterisks: implanted nanomaterial; blue arrows: newly formed spongy bone. The scale bars in panels (A, C, E, G, I, K, M, O, and Q) = 1 mm, panels (N, P, and R) = 100 μm, panels (B, D, F, H, J, and L) = 50 μm.

(Fig. 4C). The changes of the GO-implanted group were similar to the g-C₃N₄-implanted group, but the direction of osteoregeneration was centripetal and there was less newly formed woven bone with more scaffold material (Fig. 4E,F).

At 8 weeks, the control defects were still filled with fatty bone marrow (Fig. 4G,H). The bone defect in the g-C₃N₄ implanted group contained more regenerated bone tissues with less residual scaffold materials compared to the GO implanted group. The residual materials were surrounded and separated by osteoid tissue and an anastomosing network of newly formed woven bone trabeculae which annealed to the peripheral spongy bone. Moreover, lymphoid aggregation and neovascularization were observed in the implanted bone defect area (Fig. 4I–L).

At 12 weeks, the control group remained poorly repaired and bone formation could not be seen (Fig. 4M,N). However, more anastomosing networks of the newly formed woven and lamellar bone trabeculae could be seen in the implanted area and connected to the peripheral spongy bone in the g-C₃N₄ implanted group than that in the GO implanted group. Inflammatory cell infiltration and neovascularization were still seen in the implanted bone defect area. At the same time, the materials were further degraded (Fig. 4O–R).

The bone defects were further evaluated using Crossmon's trichrome and Sirius red staining (Fig. 5). The bone defects remained unrepaired in the center of the control group with the formation of newly formed bone containing mature collagen at the periphery. However, the deposition of mature collagen at the newly formed bone matrix was found in the central and peripheral regions of the bone defects in both g-C₃N₄ and GO implanted groups. Clearly, the amount of mature collagen in the newly formed bone was higher in g-C₃N₄ implanted group than the GO group (Fig. 5).

In addition, the defects were stained with PAS and hematoxylin (Fig. supp 5). The stained sections showed no chondrocytes. However, PAS-negative osteogenic cells, osteoblasts, and osteocytes in addition to PAS-positive bone matrix could be seen in the peripheral zone of all bone defects and the central zone of the implanted groups.

Histomorphometric analysis. In general, the Os% in the g-C₃N₄ and GO implanted defects displayed a highly significant difference ($P < 0.05$) compared with the control defect throughout the experiment (Fig. 6A). At 4 weeks, the Os% in g-C₃N₄ implanted defects ($54.30 \pm 5.71\%$) was significantly higher than in the GO implanted group ($39.69 \pm 6.56\%$) ($P < 0.05$). Both g-C₃N₄ and GO implanted groups displayed no significant difference at week 8 and week 12 after implantation (Fig. 6A).

The Col% in the defects implanted with g-C₃N₄ and GO were significantly higher than the control defects throughout the different implantation times ($P < 0.05$) (Fig. 6B). On weeks 4, 8, and 12 after implantation, the g-C₃N₄ implanted defects showed Col% of $21.69 \pm 3.51\%$, $31.60 \pm 5.29\%$, and $34.36 \pm 2.07\%$, respectively compared to $20.84 \pm 1.85\%$, $30.87 \pm 2.33\%$, and $32.93 \pm 4.04\%$, respectively in the GO group (Fig. 6B).

The RM% was significantly lower in g-C₃N₄ treated defects ($45.07 \pm 5.69\%$) than GO treated defects ($59.98 \pm 6.60\%$) at week 4 after implantation ($P < 0.05$). However, no significant differences were detected at weeks 8 and 12 after implantation of the nanomaterials (Fig. 6C).

Furthermore, in g-C₃N₄ and GO implanted groups, the Os% and Col% were significantly lower ($P < 0.05$) at week 4 after implantation compared to weeks 8 and 12. However, the RM% was considerably higher at week 4 after implantation than weeks 8 and 12 ($P < 0.05$) (Fig. 6).

IHC of CD34. CD34+ mesenchymal stem cells were numerous and formed a network of interconnected cells surrounding the g-C₃N₄ implanted material, whereas they were less numerous in the GO implanted group (Fig. supp 6).

qPCR analysis. The mRNA expression of OC and OP in all implanted groups revealed a higher level on week 4 after implantation, then decreased dramatically over time. OC expression was higher in g-C₃N₄ and GO implanted defects than in the control group on week 4 after implantation ($P < 0.05$), while it displayed a significance between g-C₃N₄ implanted defects and control one on week 8 ($P < 0.05$) (Fig. 7A). However, g-C₃N₄ and GO implanted groups showed non-significant differences between each other at different evaluation times (Fig. 7A).

OP expression level was higher in g-C₃N₄ and GO implanted defects compared to that in the control group at week 4 and week 8 after implantation ($P < 0.05$) (Fig. 7B). Additionally, the g-C₃N₄ implanted group showed a significance with GO implanted group at week 4 post-implantation ($P < 0.05$) (Fig. 7B).

The expression levels of OC and OP of g-C₃N₄ and GO implanted defects were significantly higher at week 4 than weeks 8 and 12 after implantation. Moreover, OP expression was higher at week 8 after implantation than week 12 (Fig. 7).

Discussion

As a health burden, critical-sized bone defects represent one of the leading causes of disability, resulting in a decline in life quality². Bone tissue engineering is an emerging field that serves to construct bone substitutes to overcome the shortcomings of conventional treatments of bone defects⁶. Even though several studies have reported the fabrication of different tissue-engineered bone grafting scaffolds to accelerate the bone healing process, the ideal material has not been developed yet^{3–5}. In the present study, we tested the biocompatibility and the bone regeneration capacity of g-C₃N₄ and GO scaffolds in vitro and in vivo.

Herein, g-C₃N₄ was synthesized via direct pyrolysis of melamine because it is a rapid and economical process⁴⁷. While GO was synthesized in this study via exfoliation using the Hummer method, which is simple, low-cost, efficient, stable over 3–5 months, and environmentally friendly procedure¹⁶. The results of XRD revealed a sharp reflection peak at the position of 27.4° ($d \sim 0.33$ nm) that matches the predicted (20) diffraction of g-C₃N₄. This finding is similar to the XRD patterns of g-C₃N₄ reported in other studies^{15,47,48}. In the diffractogram of GO, the diffraction peak at Bragg angle 12.0° refers to the Miller index (002), whereas the diffraction peak at 26.5° refers to residual graphite or re-stacking layers of the exfoliated GO^{16,17}.

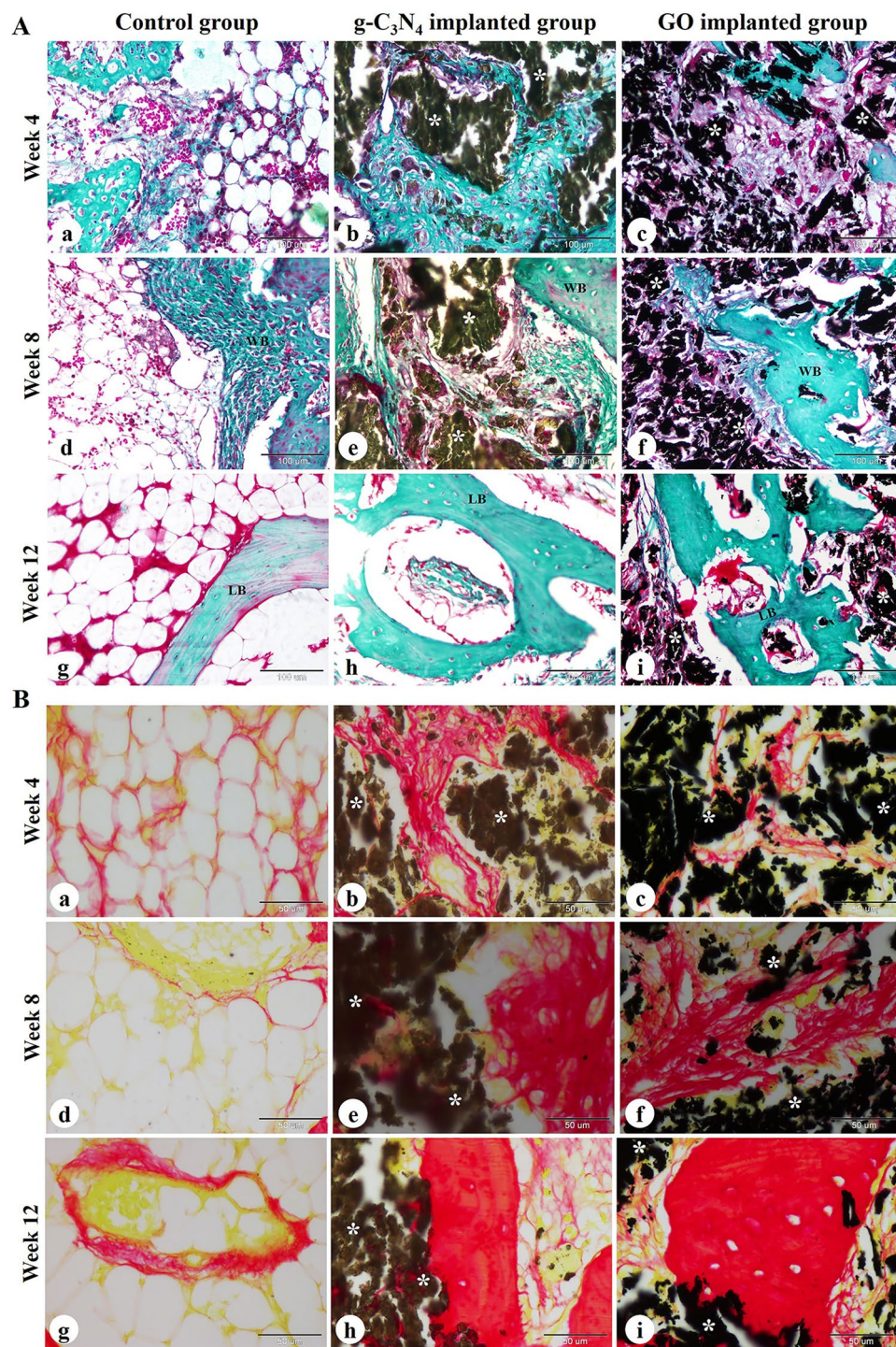


Figure 5. Histochemical evaluation of femoral condyle defect in rabbits. The repair site of the femoral condyle at weeks 4, 8, and 12 after surgery in control (a, d, g), g-C₃N₄ implanted (b, e, h), and GO implanted groups (c, f, i) was stained with Crossmon's trichrome (A) and Sirius red (B) stains. WB woven bone, LB lamellar bone; white asterisks: implanted nanomaterial. The scale bars in Crossmon's trichrome stain panels = 100 μ m, Sirius red stain panels = 50 μ m.

The cytocompatibility of the designed biomaterials is a key criterion to confirm their ability to support the host bone cell growth and adhesion for in vivo orthopedic applications⁷. Hence, in this study hFOB cells have been cultured on extracts of g-C₃N₄ and GO nanomaterials to test their cytotoxicity¹⁶. Our results revealed a non-toxic effect of g-C₃N₄ and GO nanomaterials on hFOB cells, indicating that they are cytocompatible and their use as

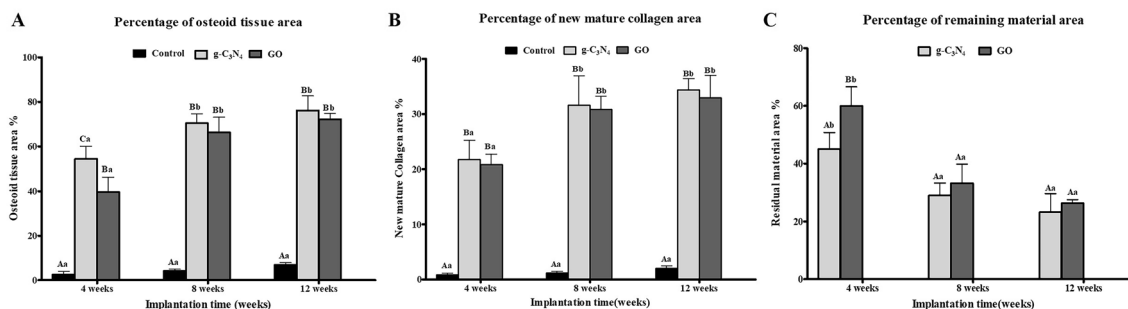


Figure 6. In vivo histomorphometrical analysis. The percentages of osteoid tissue area (A), residual material area (B), and new mature collagen area (C) to the total defect area in rabbit femoral condyle defects implanted with g-C₃N₄ and GO or left empty at various times post-implantation. Error bars \pm SD; n = 3 for each group and time point. Bars with the same letter represent values that are not significantly different (two-way ANOVA followed by Tukey's HSD post hoc test). (A–C) significance between groups; a, b, and c: significance between time points within the same group.

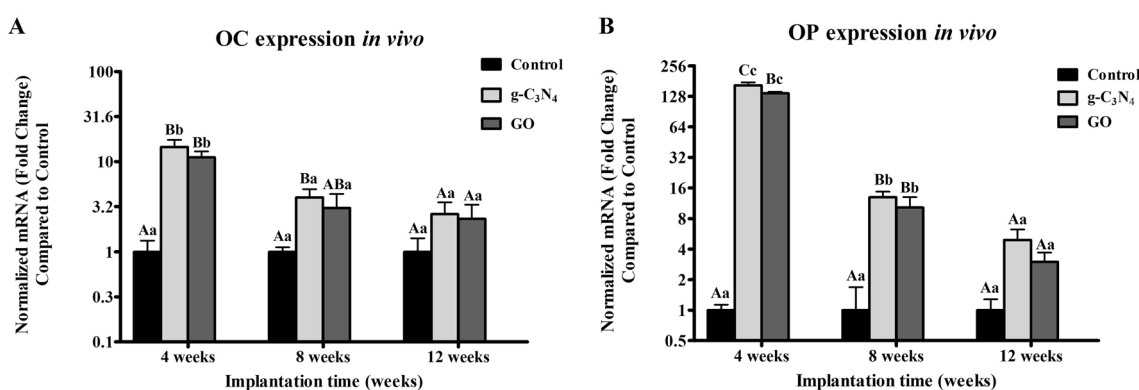


Figure 7. In vivo qRT-PCR analysis. q-PCR analysis for mRNA expression of osteocalcin (OC) (A) and osteopontin (OP) (B) in different groups at week 4, 8, and 12 post-implantations. Error bars \pm SD; n = 3 for each group and time point. Bars with the same letter represent values that are not significantly different (two-way ANOVA followed by Tukey's HSD post hoc test). (A–C) significance between groups; a, b, and c: significance between time points.

orthopedic scaffolds would not affect the normal physiological microenvironment after in vivo implantation. These findings are in agreement with Tiwari et al.¹⁵ and Hussein et al.¹⁶. Tiwari et al.¹⁵ reported high viability of HeLa cells upon culture on C₃N₄, for 24 h, while Hussein et al.¹⁶ showed good viability of human endothelial cells, hFOB cells, and mouse embryonic fibroblasts after seeding on GO for 7 days. Since the biomaterial would come in contact with blood directly after implantation, hemocompatibility testing is critical. In the current study, both g-C₃N₄ and GO nanomaterials displayed a non-hemolytic effect, indicating excellent hemocompatibility of the designed nanomaterials as reported previously^{16,49}.

The potential of biomaterials to enhance bone cell function is another key criterion in bone tissue engineering. Both g-C₃N₄ and GO showed a significant upregulation of Col-I, OC, and OP expressions, whereas the g-C₃N₄ nanomaterial showed the highest expression of the osteogenic proteins especially in the early stages of healing. These proteins play an essential role in osteoblast proliferation and differentiation, bone mineralization, and bone remodeling^{50–55}. Collectively, our data indicated that the designed nanomaterials could stimulate the osteoblast's biological activities and functions in vitro. This observation may be attributed to the material's ability to induce the expression of Runx2 that interacts with the promoter regions of osteoblast-specific genes, including Col-I, OC, and OP^{15,37,56}. Interestingly, a sharp decline in OC and OP expression on day 21 was observed, which may be caused by the complete mineralization of cells, as suggested previously^{57–60}.

To further confirm the in vitro results, we implanted the designed materials in a well-established critical-sized femoral condyle bone defect model (\varnothing 5 \times 10 mm) in rabbits^{61,62}. In this study, only male rabbits were used for investigating the in vivo behaviour of the materials to avoid the influence of female sex hormones on bone healing^{63,64}. Additionally, males are superior to females in bone regeneration due to the higher MSCs quantity as reported previously⁶³. Moreover, Pien et al., recorded a better osseointegration with larger peri-implant bone volume after 30 days in male rats compared to females⁶⁵. The interaction between the host cells and the implanted materials activates the osteogenesis process. The implantation of biomaterials causes a foreign body response, which is characterized by infiltration of different inflammatory cells and fibrosis of the surrounding tissues^{8,66}. However, our results showed mild infiltration of the inflammatory cells, e.g., macrophages, in both g-C₃N₄ and GO implanted groups, confirming their high biocompatibility and favorably creating an osteogenic milieu that

can improve osteogenesis. Inflammatory cell infiltration, particularly macrophages, is crucial for the biodegradation of the implanted materials⁶⁷. Our results showed that both g-C₃N₄ and GO were biodegraded gradually over time. However, the g-C₃N₄ implanted defects displayed the lowest percentage of residual materials.

In addition, growth factors such as bone morphogenetic proteins (BMPs), transforming growth factor β (TGF- β), and vascular endothelial growth factor (VEGF), and cytokines such as tumor necrosis factor- α (TNF- α), interleukin 1- β (IL1- β), IL-6, and IL-10, are secreted by macrophages^{8,11,66} to stimulate the osteogenesis process via migration of the undifferentiated MSCs with osteogenic potential from the bone marrow and peripheral blood and eventually differentiation, osteoblast maturation, collagen organization and mineralization^{8,66,68,69}. MSCs migrated through the disintegrated scaffold materials to the center of the defect have a crucial role in bone regeneration and remodeling by providing a favorable environment with the ability to differentiate into osteoblasts and stimulate the production of several growth factors that promote the osteogenesis process^{70–74}. Therefore, osteogenesis has been promoted in g-C₃N₄ and GO implanted groups, where MSCs differentiated to osteogenic cells and then to osteoblasts. Osteoblasts synthesize and secrete bone collagen and bone matrix, then transform into osteocytes. Finally, the newly formed woven bone remodels into lamellar bone^{75,76}.

Our results showed the formation of immature woven bone, which was remodeled later to mature lamellar bone in the g-C₃N₄ and GO implanted defects. However, the new bone formation was significantly higher in the g-C₃N₄ group than in the GO. These differences are attributed to the properties of the materials including chemical composition, structure, and porosity. g-C₃N₄ is a polymeric material containing elements of C, N, and H, while GO is 2D materials of C, O, and H. Compared with the GO, g-C₃N₄ has electron-rich materials with basic surface properties. It offers H-bonding motifs enabling hydrogen bond formation with biomolecules inside the bone. The functional properties of g-C₃N₄ exhibit higher interconnectivity to proteins helps in the transfer of nutrients and elimination of metabolic waste, making the scaffold a more conducive milieu for MSCs attachment, growth, and proliferation⁸. Moreover, CD³⁴⁺ cells were detected surrounding the implanted material. CD³⁴⁺ was reported as a common marker for MSCs that can differentiate into osteoblasts *in vitro*^{72,77,78}.

For investigating the *in vivo* capability of the designed nanomaterials to promote *de novo* bone formation at a molecular level, the expressions of osteogenic genes (OC and OP) were analyzed. Our results demonstrated upregulated expressions of these genes in both implanted groups. The power of the fabricated nanomaterials for OC and OP upregulation suggested to be related to their potential to induce canonical Wnt signaling^{15,37}. The functional groups in g-C₃N₄ and GO stimulate the ligand Wnt3a to bind with the receptor lipoprotein receptor-related proteins-5 (LRP5), followed by an increase the intracellular Axis inhibition protein-2 (AXIN-2) and Catenin Beta (CTNNB) gene expressions leading to upregulation of the osteogenic regulators (Runx2, Distal-less homeobox 5 (Dlx5), and Osterix (Osx)) and consequently enhanced the osteogenesis^{15,37,79}. Notably, mRNA expressions of OC and OP in the g-C₃N₄ and GO implanted groups displayed abrupt downregulation at weeks 8 and 12 after implantation; this might be related to the normal decrease in the production of bone matrix proteins in the late stages of bone healing^{80,81}. Moreover, the overexpression of OP on week 4 after implantation in the different implanted groups may be attributed to its secretion by macrophages and osteoblast lineage cells⁸².

In conclusion, the g-C₃N₄ and GO are biocompatible nanomaterials with the potential to upregulate osteoblast's marker genes *in vitro* in hFOB. They provide a suitable *in vitro* and *in vivo* environment for stimulating cellular migration, proliferation, adhesion, and differentiation. In addition, they have a robust anabolic effect on the regeneration process of critical-sized bone defect in rabbits. Lastly, our data suggest the possibility to use g-C₃N₄ and GO biomaterials as promising bone substitutes for reconstructing the osseous defects that cannot heal naturally.

In the current study, it is worth mentioning that there were few limitations such as the use of small sample size and insufficient characterization of the materials in terms of porosity and biodegradation. Future studies should focus on the biomechanical characteristics and biodegradation of g-C₃N₄ and GO nanomaterials as promising scaffolds for bone tissue regeneration. In addition, the fate of g-C₃N₄ and GO degradation byproducts must be investigated in further studies. Moreover, future research is needed to be conducted on a large scale to compare the bone regenerative capacity of both g-C₃N₄ and GO nanomaterials relative to other previously well-known established scaffolds such as tricalcium phosphate, demineralized bone matrix, and hydroxyapatite.

Materials and methods

Materials. Melamine was purchased from Acros organics (Belgium) with a purity of $\geq 98\%$, and flake graphite (average particle diameter of 20 μm , 99.95% purity) was purchased from Alfa Aesar (Germany). Nitric acid (69–72%) and sulfuric acid (96.0%) were purchased from ElNaser company (Egypt).

Synthesis of g-C₃N₄. The g-C₃N₄ was synthesized via the pyrolysis of melamine¹⁵. Typically, 10 g of melamine was placed in a crucible with a cover. The crucible was then placed in a muffle furnace and heated to 550 °C for 5 h with a heating rate of 2 °C/min under atmospheric nitrogen pressure. After the heating reaction, the crucible was left to cool down to room temperature in the furnace. The product was washed with absolute ethanol and distilled deionized water (3 \times 50 mL) and dried at 80 °C for 24 h. A solution (1 mg/mL) of the designed material was prepared via ultrasonication dispersion overnight.

Synthesis of GO. GO was prepared using a modified Hummers method¹⁶. Briefly, a mixture of nitric acid (10 mL) and sulfuric acid (15 mL) was added to graphite (1 g). The solution flask was soaked in ice to keep the temperature below 0 °C. Three grams of potassium permanganate were added into the reaction mixture that was stirred for 12 h. Then, hydrogen peroxide (30–32%, 15 mL) was added dropwise to remove the excess permanganate. The material was filtered and washed several times with water and diluted HCl to remove any metals. The GO (20 mg) solution was prepared via ultrasonic dispersion in water (20 mL).

Materials characterization. The morphology and size of these nanomaterials were studied using a transmission electron microscope (TEM; JEM-2100, JEOL, Japan). The phase purity of the prepared materials was characterized using X-ray powder diffraction (XRD; Philips 1700 diffractometer, Germany) with a Cu K α radiation diffractometer. Scanning electron microscopy (SEM) and energy-dispersive X-ray spectroscopy (EDS) were recorded by TM3000 (Hitachi, Japan). Raman spectrum for GO dispersion was measured using the Horiba Labram HR system (wavelength of 785 nm and power of 150 mW). The zeta potential of the GO colloidal was evaluated using Zetasizer (Malvern, UK).

Indirect contact cytotoxicity assay. Extracts of materials were prepared to evaluate the potential toxic risk of leaching chemicals. The extracts of the g-C $_3$ N $_4$ and GO were prepared via incubating samples in the serum-free 1:1 mixture of Ham's F12 and Medium Dulbecco Modified Eagle's minimal essential medium (DMEM) supplemented with 1% penicillin/streptomycin (p/s, Gibco; Grand Island, NY, USA) culture medium under the condition of 37 °C/120 r/min for 72 h, according to a ratio standard of 0.2 g/mL of culture medium⁶⁷. The supernatant was withdrawn and centrifuged to prepare the conditioned extracts, then filtered using 0.4 μ m filters and stored at 4 °C till performing the cytotoxicity test. Human fetal-osteoblast cell line (hFOB 1.19; American Type Culture Collection (ATCC), USA) was cultured in a 1:1 mixture of Ham's F12 and DMEM supplemented with 10% fetal bovine serum (FBS, Hyclone; Logan, UT, USA) and 2.5 mM L-glutamine (Gibco) and 1% p/s in a humidified incubator at 34 °C and 5% CO $_2$. At 70% confluency, the cells were harvested via trypsinization. The cells were placed at a density of 15×10^3 in a 48-well plate for 24 h using the complete culture medium, then the medium was aspirated, followed by the addition of 500 μ L conditioned or control medium after adding 10% FBS. In the negative control group, cells were cultured with complete medium only, while the cells were cultured in the presence of 20% dimethyl sulfoxide (DMSO) in the positive control. The cell response against the extracts was evaluated after incubating the plate for 1, 3, and 7 days. To measure the metabolic activity of cells, [3-(4,5-dimethylthiazol)-2-yl]-2,5-diphenyltetrazolium bromide (MTT) assay was performed. Briefly, 50 μ L of MTT solution (5 mg/mL, Sigma-Aldrich, St Louis, MO, USA) was added to each well and incubated at 37 °C for 4 h. After discarding the medium containing MTT, 250 μ L DMSO was added to all wells to dissolve the formazan into a purple solution. After 10 min of incubation, 100 μ L aliquots from the wells were pipetted into another 96-well plate. The color developed was quantified by recording the absorbance at a wavelength of 570 nm with a spectrophotometer. The cell activity was represented as the percentage of activity expressed by cells compared to the negative control.

To qualitatively assess the cell viability after 7 days, staining with a Live/Dead assay kit (calcein-AM/ethidium Bromide homodimer, Invitrogen, USA) according to the manufacturer's instructions, then imaged using a fluorescence microscope (Olympus, Tokyo, Japan).

Hemocompatibility evaluation using hemolysis assay. The hemolysis that may occur due to contact of materials with blood was measured according to Momtahan et al.⁸³. Briefly, 10 mL of fresh blood was collected from 7 dogs and directly transferred to the laboratory. Erythrocytes were separated by centrifuging at 2000 \times g for 15 min, followed by dilution in 1 \times phosphate buffer saline (PBS) to create an erythrocyte suspension with 2×10^9 cells/mL. A sample of each nanomaterial was placed in a glass tube containing 5 mL of erythrocyte suspension and kept at room temperature on a shaker with 125 rpm for 60 min. Afterward, 1 mL of the suspension was collected from each tube and centrifuged for 3 min at 3000 \times g. Erythrocyte suspension without any specimens was utilized as a negative control, whereas tubes containing 25 mg of sodium dodecyl sulfate (SDS) added to the erythrocytes were used as positive controls. Finally, the absorbance of the supernatant was examined at a wavelength of 545 nm using a spectrophotometer, and the hemolysis percentage was calculated as in the equation:

$$\text{Hemolysis(\%)} = \frac{S545 - N545}{P545 - N545} \times 100,$$

where the absorbance for samples, negative control, and positive control were represented by S545, N545, and P545, respectively.

Quantitative polymerase chain reaction (qPCR) analysis. The nanomaterials were placed into 48-well plates to investigate the ability of the materials to enhance the attachment of hFOB 1.19 cells. Shortly, cell suspension containing 10×10^3 cells (500 μ L) was added on the surface of the powder, and the plate was incubated at 34 °C in 5% CO $_2$ for 28 days. After 3, 7, 14, 21, 28 days of culture, qPCR analysis for collagen type-I (Col-I), osteocalcin (OC), and osteopontin (OP) expressions were performed as in previous studies^{61,84}. At the different evaluation times, total RNA was isolated from the cultured cells and transcribed into cDNA using the NucleoSpin RNA Mini kit (Macherey–Nagel GmbH & Co., Germany) and TOPscrip RT DryMIX (Enzynomics, South Korea), respectively. Quantitative real-time PCR was carried out using TOPreal qPCR 2 \times PreMIX (Enzynomics, South Korea) on a StepOnePlus real-time PCR system (Thermo Fisher Scientific) according to the manufacturer's instructions. The relative expression was calculated by the comparative Ct (2 $^{-\Delta\Delta C_t}$) method with glyceraldehyde 3-phosphate dehydrogenase (GAPDH) as the internal control. The primer sequences used are listed in Table 1.

In vivo critical-sized bone defect model. The critical-sized bone defect model was carried out in rabbit femoral condyles for assessing the ability of g-C $_3$ N $_4$ and GO to stimulate bone regeneration. Animal experiments were approved by the Institutional Animal Care and Use Committee of Research Facilities, Faculty of Veterinary Medicine, Assiut University, Egypt according to the Egyptian bylaws, OIE standards, and the Animal

Research: Reporting of In Vivo Experiments (ARRIVE) guidelines for use of animals in research (Approval number: 06/2023/0025). All methods were performed in accordance with the relevant guidelines and regulations. In this experiment, 54 male New Zealand white rabbits (6 months, 2.5–3.0 kg) were used. They were housed in single stainless-steel cages in a well-ventilated room and maintained on a standard commercial rabbit chow diet and access to water was ad libitum. The animals' hindlimbs were examined radiographically prior to surgery to ensure the skeletal maturity of the animals and normal bone anatomy. Rabbits were acclimatized for 2 weeks before the surgical procedure at their new housing units. Animals were randomly classified into three groups (n = 18 for each group); the control group, the g-C₃N₄ group, and the GO group.

Rabbits were subjected to food starvation for 8 h before surgery with free access to water. All surgical procedures were conducted under general anesthesia and strict aseptic conditions. Animals were anesthetized using a combination of xylazine HCl (3 mg/kg, Xyla-ject 20%: ADWIA Co., Egypt) and ketamine HCl (40 mg/kg, Ketamine 50%: Sigma-Tec, Egypt), and maintained using isoflurane (2.5–3%, Forane: AbbVie, England) in oxygen (2 L/minute) throughout the surgery. Following induction of general anesthesia, the right hindlimb was prepared aseptically and draped. A critical-sized bone defect model of 5 mm in diameter and 10 mm in depth was induced in right lateral femoral condyles⁶². Briefly, a lateral parapatellar 5 cm skin incision was performed on each lateral femoral condyle, then the underlying fascia was dissected parallel to the skin incision and the femoral shaft. The femoral condyle was consequently exposed by extending the muscle fibers, and the overlying periosteum was removed. A unicortical cylindrical defect was created using a trephine burr in the center of each femoral condyle. Drilling was done using a dental micromotor with low-speed contra (Strong, Korea) and trephine burrs with continuous physiological saline irrigation to minimize thermal damage and prevent bone necrosis. Firstly, a confined cancellous defect was stepwise drilled with a trephine burr (Ø = 3 mm; Osung, Korea) perpendicular to the long axis of the femoral shaft. Then, the defects were expanded with a larger trephine burr (Ø = 5 mm; Oxy, Italy), eventually creating a critical-sized defect (Ø 5 × 10 mm). The bleeding was controlled by applying firm pressure with sterile gauze for 3–5 min. The defect was thoroughly irrigated with normal saline and dried with sterile gauze to remove debris. Then, the defects were left empty as a control group or implanted randomly with the different scaffolds (g-C₃N₄ or GO). At last, muscle attachment, subcutaneous tissue, and skin were routinely sutured in layers. After surgery, subcutaneous administration of meloxicam (0.6 mg/kg; Mobitil, MUP, Egypt) and penicillin (40 mg/kg; Pen & Strep, Norbook, Egypt) was carried out for five consecutive days to relieve pain and prevent infection, respectively. Animals were allowed to move inside their cages without restriction and given their traditional regimen of food and water a few hours after the operation. Rabbits were sacrificed after 4, 8, and 12 weeks of surgery (n = 6 rabbits for each time point in each group), and samples were harvested for evaluation of bone repair.

Clinical observation. All animals were subjected to the daily clinical examination of any surgical complications, including evidence of infection and wound dehiscence. Additionally, the health condition of animals was recorded, including activity level, gait, and mobility of the hindlimbs.

Radiographical assessment. Rabbit femoral condyles were radiographed to evaluate new bone formation in bone defects based on radiopacity changes in central and peripheral areas of the defects. Latero-medial (LM) radiographs were obtained immediately after surgery (baseline) as well as at week 4, week 8, and week 12 postoperatively. LM radiographs were taken using an ultra-high-definition film and fixed X-ray apparatus (Philips Super 80 CP, Germany). Radiographs were compared for bone density based on the mean grayscale value per unit area of defects using ImageJ 1.52 software (National Institute of Health, USA, n = 3 for each group at each time point) as reported by Liu et al.⁸⁵.

Computed tomography (CT) scanning. Femoral condyle bone defects were radiographed using CT scanning at week 12 using CT apparatus (120 kV and 53 mA/s, 1 mm thickness; Philips 128 slice scanner, Germany). Coronal, sagittal, and transverse images were obtained as well as lateral 3D-CT images to evaluate the bone regeneration at the defect regions.

Primer	Primer sequences	
	Forward	Reverse
Human collagen-I	5'-CAG CCG CTT CAC CTA CAG C-3'	5'-TTT TGT ATT CAA TCA CTG TCT TGC C-3'
Human osteocalcin	5'-ACA CTC CTC GCC CTA TTG-3'	5'-GAT GTG GTC AGC CAA CTC-3'
Human osteopontin	5'-CTC AGG CCA GTT GCA GCC-3'	5'-CAA AAG CAA ATC ACT GCA ATT CTC-3'
Human GAPDH	5'-ACA GTC AGC CGC ATC TTC TT-3'	5'-GAC AAG CTT CCC GTT CTC AG-3'
Rabbit osteopontin	5'-GCTCGATGGCTAGCTTGCT-3'	5'-ACAATATAAGCGGAGGCCA-3'
Rabbit osteocalcin	5'-GTTCCCTTCTCTTGATT-3'	5'-TCTACCAGTGCAGCCTGAC-3'
Rabbit beta-actin	5'-CAGGAAGGAGGCTGGAACA-3'	5'-ATCGTGCGGGACATCAAGGA-3'

Table 1. List of primer sequences used for in vitro and in vivo osteogenic gene expression analysis.

Gross examination of the bone defects. After sacrificing animals at different time points, the femurs were resected. All tissues were stripped for gross examination of the femoral condyles to evaluate scaffold incorporation and new bone formation.

Histological examination. Femoral condyle samples ($n = 3$ for each time point) were collected and fixed in 10% neutral buffered formalin. The samples were then decalcified in 25% formic acid for 30 days at 37 °C and a pH of 7.0, dehydrated in ascending grades of ethanol, cleared in methyl benzoate, embedded in paraffin, and sectioned at 5 μm in thickness. The slides were then stained with hematoxylin and eosin (H&E) to analyze the bone formation, the response of the graft materials, and the local tissue reaction through observation of the cellular components, neovascularization, and general structure in the defect site⁸⁶. Moreover, histochemical staining of bone collagen was performed using Crossmon's trichrome staining to examine the bone collagen fibers formation within the defect area⁸⁶, and Sirius red staining to differentiate between mature and immature bone collagen⁸⁷. Additionally, Periodic acid-Schiff (PAS) staining was used for demonstration of neutral mucopolysaccharide⁸⁸. Afterward, the slides were examined under the microscope (Olympus BX51, Japan) and photographed using a digital camera (Olympus DP72, Japan). The histological interpretation was performed blindly on coded samples and compared with the control group.

Histomorphometric analysis. The percentage of osteoid tissue area (Os%) and residual material area (RM%) were measured in the H&E-stained slides ($n = 3$), whereas the percentage of newly formed mature bone collagen area (Col%) was calculated in Sirius red-stained sections ($n = 3$). The area of osteoid tissue, the area of newly formed mature bone collagen, and the area of residual material were outlined using threshold area fraction in a specified region of interest (ROI, the entire defect area: a rectangular of 25.6 mm^2) using ImageJ software^{61,62,89}. The Os%, Col%, and RM% were reported as a percentage of the entire defect area, expressed as mean \pm SD, and calculated as follows:

$$\text{Os \%} = \text{Os}/\text{ROI} \times 100, \text{Col \%} = \text{Col}/\text{ROI} \times 100, \text{RM \%} = \text{RM}/\text{ROI} \times 100,$$

where the osteoid tissue area, newly formed mature collagen area, and residual material area were represented by Os, Col, and RM, respectively.

Immunohistochemical evaluation (IHC). IHC detection of CD34 in paraffin sections was performed at week 12 as described previously⁹⁰ using CD34 monoclonal antibody (Catalog Number: CM 084 A, B, C, Biocare Medical, USA) and ultravision one detection system HRP polymer and AEC chromogen (Catalog Number: TL-015-HAJ, Thermo Fisher Scientific, USA).

Quantitative real-time PCR (qRT-PCR) analysis. Three samples were harvested from each group on weeks 4, 8, and 12 after surgery for qRT-PCR analysis. After dissection of soft tissues and periosteum, samples were removed carefully using a trephine under strict aseptic conditions and then immediately submerged in RNA later solution (Thermo Scientific, USA) and frozen at -80 °C for later processing. The stored frozen samples were ground under liquid nitrogen using mortar for RNA isolation. Total RNA was isolated from the samples using the TRIzol Reagent (Life Technologies) according to the manufacturer's protocol. Then, reverse transcription and qRT-PCR were performed as previously mentioned for OC and OP. The primer sequences used are listed in Table 1.

Statistical analysis. Data were analyzed with a statistical software (IBM SPSS version 21). The data are presented as a mean \pm standard deviation (SD) at a significant level of $p < 0.05$. The results of cytotoxicity assay ($n = 8$), hemocompatibility, and in vitro Col-I, OC, and OP expressions ($n = 3$ for each time point in each group), were compared by one-way ANOVA, followed by Tukey's test. The results of bone density, Os%, Col%, RM%, and in vivo OC and OP expressions ($n = 3$ for each time point in each group) were analyzed by two-way ANOVA, followed by Tukey's test.

Data availability

The data that support the findings of this study are available from the corresponding author upon reasonable request.

Received: 14 March 2022; Accepted: 28 March 2023

Published online: 03 April 2023

References

- Schemitsch, E. H. Size matters: Defining critical in bone defect size!. *J. Orthop. Trauma* **31**, 1–10 (2017).
- Wang, P. *et al.* Bone tissue engineering via nanostructured calcium phosphate biomaterials and stem cells. *Bone Res.* **2**, 14017–14017. <https://doi.org/10.1038/boneres.2014.17> (2014).
- Liu, X., Shen, H., Song, S., Chen, W. & Zhang, Z. Accelerated biomineralization of graphene oxide: Incorporated cellulose acetate nanofibrous scaffolds for mesenchymal stem cell osteogenesis. *Colloids Surf. B* **159**, 251–258. <https://doi.org/10.1016/j.colsurfb.2017.07.078> (2017).
- Huang, Y.-H. *et al.* Three-dimensionally printed hyperelastic bone scaffolds accelerate bone regeneration in critical-size calvarial bone defects. *Plast. Reconstr. Surg.* **143**, 1397–1406 (2019).
- Xie, R. *et al.* Self-fitting shape memory polymer foam inducing bone regeneration: A rabbit femoral defect study. *Biochim. Biophys. Acta (BBA)* **1862**, 936–945. <https://doi.org/10.1016/j.bbagen.2018.01.013> (2018).

6. Zhou, T. *et al.* Electrospun poly(3-hydroxybutyrate-co-4-hydroxybutyrate)/graphene oxide scaffold: Enhanced properties and promoted in vivo bone repair in rats. *ACS Appl. Mater. Interfaces*. **9**, 42589–42600. <https://doi.org/10.1021/acsami.7b14267> (2017).
7. Wang, Q. *et al.* A graded graphene oxide-hydroxyapatite/silk fibroin biomimetic scaffold for bone tissue engineering. *Mater. Sci. Eng. C* **80**, 232–242. <https://doi.org/10.1016/j.msec.2017.05.133> (2017).
8. Chen, Z. *et al.* Osteoimmunomodulation for the development of advanced bone biomaterials. *Mater. Today* **19**, 304–321. <https://doi.org/10.1016/j.mattod.2015.11.004> (2016).
9. Nie, W. *et al.* Three-dimensional porous scaffold by self-assembly of reduced graphene oxide and nano-hydroxyapatite composites for bone tissue engineering. *Carbon* **116**, 325–337. <https://doi.org/10.1016/j.carbon.2017.02.013> (2017).
10. Rahighi, R., Panahi, M., Akhavan, O. & Mansoorianfar, M. Pressure-engineered electrophoretic deposition for gentamicin loading within osteoblast-specific cellulose nanofiber scaffolds. *Mater. Chem. Phys.* **272**, 125018. <https://doi.org/10.1016/j.matchemphys.2021.125018> (2021).
11. Xue, D. *et al.* Immunomodulatory properties of graphene oxide for osteogenesis and angiogenesis. *Int. J. Nanomed.* **13**, 5799–5810. <https://doi.org/10.2147/IJN.S170305> (2018).
12. Chimene, D., Alge, D. L. & Gaharwar, A. K. Two-dimensional nanomaterials for biomedical applications: Emerging trends and future prospects. *Adv. Mater.* **27**, 7261–7284. <https://doi.org/10.1002/adma.201502422> (2015).
13. Liao, G. *et al.* Emerging graphitic carbon nitride-based materials for biomedical applications. *Progress Mater. Sci.* **112**, 100666. <https://doi.org/10.1016/j.pmatsci.2020.100666> (2020).
14. Singh, A. *et al.* Emergence of heptazine-based graphitic carbon nitride within hydrogel nanocomposites for scarless healing of burn wounds. *ACS Appl. Polym. Mater.* **2**, 5743–5755. <https://doi.org/10.1021/acsapm.0c01020> (2020).
15. Tiwari, J. N. *et al.* Accelerated bone regeneration by two-photon photoactivated carbon nitride nanosheets. *ACS Nano* **11**, 742–751. <https://doi.org/10.1021/acs.nano.6b07138> (2017).
16. Hussein, K. H., Abdelhamid, H. N., Zou, X. & Woo, H.-M. Ultrasonicated graphene oxide enhances bone and skin wound regeneration. *Mater. Sci. Eng. C* **94**, 484–492. <https://doi.org/10.1016/j.msec.2018.09.051> (2019).
17. Soliman, M., Sadek, A. A., Abdelhamid, H. N. & Hussein, K. Graphene oxide-cellulose nanocomposite accelerates skin wound healing. *Res. Vet. Sci.* **137**, 262–273. <https://doi.org/10.1016/j.rvsc.2021.05.013> (2021).
18. Akhavan, O. Graphene scaffolds in progressive nanotechnology/stem cell-based tissue engineering of the nervous system. *J. Mater. Chem. B* **4**, 3169–3190. <https://doi.org/10.1039/C6TB00152A> (2016).
19. Abdelhamid, H. & Hussein, K. Graphene oxide as a carrier for drug delivery of methotrexate. *Biointerface Res. Appl. Chem.* **11**, 14726–14735 (2021).
20. Song, E. *et al.* Hyaluronic acid-decorated graphene oxide nanohybrids as nanocarriers for targeted and pH-responsive anticancer drug delivery. *ACS Appl. Mater. Interfaces*. **6**, 11882–11890. <https://doi.org/10.1021/am502423r> (2014).
21. Dowaidar, M., Abdelhamid, H. N., Hällbrink, M., Zou, X. & Langel, Ü. Graphene oxide nanosheets in complex with cell penetrating peptides for oligonucleotides delivery. *Biochim. Biophys. Acta* **1861**, 2334–2341. <https://doi.org/10.1016/j.bbagen.2017.07.002> (2017).
22. Wang, Y. *et al.* Functionalized folate-modified graphene oxide/PEI siRNA nanocomplexes for targeted ovarian cancer gene therapy. *Nanoscale Res. Lett.* **15**, 57. <https://doi.org/10.1186/s11671-020-3281-7> (2020).
23. Sahne, F., Mohammadi, M. & Najafpour, G. D. Single-layer assembly of multifunctional carboxymethylcellulose on graphene oxide nanoparticles for improving in vivo curcumin delivery into tumor cells. *ACS Biomater. Sci. Eng.* **5**, 2595–2609. <https://doi.org/10.1021/acsbiomaterials.8b01628> (2019).
24. Akhavan, O. & Ghaderi, E. Graphene nanomesh promises extremely efficient in vivo photothermal therapy. *Small* **9**, 3593–3601. <https://doi.org/10.1002/sml.201203106> (2013).
25. Shahnaawaz Khan, M., Abdelhamid, H. N. & Wu, H.-F. Near infrared (NIR) laser mediated surface activation of graphene oxide nanoflakes for efficient antibacterial, antifungal and wound healing treatment. *Colloids Surf. B* **127**, 281–291. <https://doi.org/10.1016/j.colsurfb.2014.12.049> (2015).
26. Abdelhamid, H. N., Khan, M. S. & Wu, H.-F. Graphene oxide as a nanocarrier for gramicidin (GOGD) for high antibacterial performance. *RSC Adv.* **4**, 50035–50046. <https://doi.org/10.1039/C4RA07250B> (2014).
27. Akhavan, O. & Ghaderi, E. Toxicity of graphene and graphene oxide nanowalls against bacteria. *ACS Nano* **4**, 5731–5736. <https://doi.org/10.1021/nn101390x> (2010).
28. Ebrahimi, M., Asadi, M. & Akhavan, O. Graphene-based nanomaterials in fighting the most challenging viruses and immunogenic disorders. *ACS Biomater. Sci. Eng.* **8**, 54–81. <https://doi.org/10.1021/acsbiomaterials.1c01184> (2022).
29. Akhavan, O., Choobtashani, M. & Ghaderi, E. Protein degradation and RNA efflux of viruses photocatalyzed by graphene-tungsten oxide composite under visible light irradiation. *J. Phys. Chem. C* **116**, 9653–9659. <https://doi.org/10.1021/jp301707m> (2012).
30. Renteria, J. D. *et al.* Strongly anisotropic thermal conductivity of free-standing reduced graphene oxide films annealed at high temperature. *Adv. Func. Mater.* **25**, 4664–4672. <https://doi.org/10.1002/adfm.201501429> (2015).
31. Ayazi, H. *et al.* Graphene aerogel nanoparticles for in-situ loading/pH sensitive releasing anticancer drugs. *Colloids Surf. B* **186**, 110712. <https://doi.org/10.1016/j.colsurfb.2019.110712> (2020).
32. Paavilainen, S., Ropo, M., Nieminen, J., Akola, J. & Räsänen, E. Coexisting honeycomb and Kagome characteristics in the electronic band structure of molecular graphene. *Nano Lett.* **16**, 3519–3523. <https://doi.org/10.1021/acs.nanolett.6b00397> (2016).
33. Kiew, S. F., Kiew, L. V., Lee, H. B., Imae, T. & Chung, L. Y. Assessing biocompatibility of graphene oxide-based nanocarriers: A review. *J. Control. Release* **226**, 217–228. <https://doi.org/10.1016/j.jconrel.2016.02.015> (2016).
34. Martín, C. *et al.* A biodegradable multifunctional graphene oxide platform for targeted cancer therapy. *Adv. Func. Mater.* **29**, 1901761. <https://doi.org/10.1002/adfm.201901761> (2019).
35. Lee, W. C. *et al.* Origin of enhanced stem cell growth and differentiation on graphene and graphene oxide. *ACS Nano* **5**, 7334–7341. <https://doi.org/10.1021/nn202190c> (2011).
36. Akhavan, O., Ghaderi, E. & Shahsavari, M. Graphene nanogrids for selective and fast osteogenic differentiation of human mesenchymal stem cells. *Carbon* **59**, 200–211. <https://doi.org/10.1016/j.carbon.2013.03.010> (2013).
37. Wu, C. *et al.* Graphene-oxide-modified β -tricalcium phosphate bioceramics stimulate in vitro and in vivo osteogenesis. *Carbon* **93**, 116–129. <https://doi.org/10.1016/j.carbon.2015.04.048> (2015).
38. Manikandan, M., Nasser Abdelhamid, H., Talib, A. & Wu, H.-F. Facile synthesis of gold nanohexagons on graphene templates in Raman spectroscopy for biosensing cancer and cancer stem cells. *Biosens. Bioelectron.* **55**, 180–186. <https://doi.org/10.1016/j.bios.2013.11.037> (2014).
39. Abdelhamid, H. N. & Wu, H.-F. Proteomics analysis of the mode of antibacterial action of nanoparticles and their interactions with proteins. *TrAC Trends Anal. Chem.* **65**, 30–46. <https://doi.org/10.1016/j.trac.2014.09.010> (2015).
40. Jiang, J. *et al.* Dependence of electronic structure of g-C₃N₄ on the layer number of its nanosheets: A study by Raman spectroscopy coupled with first-principles calculations. *Carbon* **80**, 213–221. <https://doi.org/10.1016/j.carbon.2014.08.059> (2014).
41. Nasser Abdelhamid, H., Wu, B.-S. & Wu, H.-F. Graphene coated silica applied for high ionization matrix assisted laser desorption/ionization mass spectrometry: A novel approach for environmental and biomolecule analysis. *Talanta* **126**, 27–37. <https://doi.org/10.1016/j.talanta.2014.03.016> (2014).
42. Abdelhamid, H. N. & Wu, H.-F. Ultrasensitive, rapid, and selective detection of mercury using graphene assisted laser desorption/ionization mass spectrometry. *J. Am. Soc. Mass Spectrom.* **25**, 861–868. <https://doi.org/10.1007/s13361-014-0825-z> (2014).

43. Ashour, R. M. *et al.* Rare earth ions adsorption onto graphene oxide nanosheets. *Solvent Extr. Ion Exch.* **35**, 91–103. <https://doi.org/10.1080/07366299.2017.1287509> (2017).
44. Akhavan, O. Bacteriorhodopsin as a superior substitute for hydrazine in chemical reduction of single-layer graphene oxide sheets. *Carbon* **81**, 158–166. <https://doi.org/10.1016/j.carbon.2014.09.044> (2015).
45. Kurniasari, *et al.* Defect and magnetic properties of reduced graphene oxide prepared from old coconut shell. *IOP Conf. Ser.* **196**, 012021. <https://doi.org/10.1088/1757-899x/196/1/012021> (2017).
46. Abdelhamid, H. N. & Wu, H.-F. Reduced graphene oxide conjugate thymine as a new probe for ultrasensitive and selective fluorometric determination of mercury(II) ions. *Microchim. Acta* **182**, 1609–1617. <https://doi.org/10.1007/s00604-015-1461-4> (2015).
47. Li, X. *et al.* Preparation and characterization of graphitic carbon nitride through pyrolysis of melamine. *Appl. Phys. A* **94**, 387–392. <https://doi.org/10.1007/s00339-008-4816-4> (2009).
48. Abdellah, A. R., Abdelhamid, H. N., El-Adasy, A.-B.A.A.M., Atalla, A. A. & Aly, K. I. One-pot synthesis of hierarchical porous covalent organic frameworks and two-dimensional nanomaterials for selective removal of anionic dyes. *J. Environ. Chem. Eng.* **8**, 104054. <https://doi.org/10.1016/j.jece.2020.104054> (2020).
49. Yadav, P., Zhang, C., Whittaker, A. K., Kailasam, K. & Shanavas, A. Magnetic and photocatalytic curcumin bound carbon nitride nanohybrids for enhanced glioma cell death. *ACS Biomater. Sci. Eng.* **5**, 6590–6601. <https://doi.org/10.1021/acsbomaterials.9b01224> (2019).
50. Fonseca, H., Moreira-Gonçalves, D., Coriolano, H.-J.A. & Duarte, J. A. Bone quality: The determinants of bone strength and fragility. *Sports Med.* **44**, 37–53. <https://doi.org/10.1007/s40279-013-0100-7> (2014).
51. Lin, X., Patil, S., Gao, Y.-G. & Qian, A. The bone extracellular matrix in bone formation and regeneration. *Front. Pharmacol.* <https://doi.org/10.3389/fphar.2020.00757> (2020).
52. Midha, S., Murab, S. & Ghosh, S. Osteogenic signaling on silk-based matrices. *Biomaterials* **97**, 133–153. <https://doi.org/10.1016/j.biomaterials.2016.04.020> (2016).
53. Mizokami, A., Kawakubo-Yasukochi, T. & Hirata, M. Osteocalcin and its endocrine functions. *Biochem. Pharmacol.* **132**, 1–8. <https://doi.org/10.1016/j.bcp.2017.02.001> (2017).
54. Sartori, M. *et al.* Collagen type I coating stimulates bone regeneration and osteointegration of titanium implants in the osteopenic rat. *Int. Orthop.* **39**, 2041–2052. <https://doi.org/10.1007/s00264-015-2926-0> (2015).
55. Singh, A., Gill, G., Kaur, H., Amhmed, M. & Jakhu, H. Role of osteopontin in bone remodeling and orthodontic tooth movement: A review. *Prog. Orthod.* **19**, 18. <https://doi.org/10.1186/s40510-018-0216-2> (2018).
56. Kirkham, G. & Cartmell, S. Genes and proteins involved in the regulation of osteogenesis. *Top. Tissue Eng.* **3**, 1–22 (2007).
57. Kaur, G. *et al.* Regulation of osteogenic differentiation of rat bone marrow stromal cells on 2D nanorod substrates. *Biomaterials* **31**, 1732–1741. <https://doi.org/10.1016/j.biomaterials.2009.11.041> (2010).
58. Lin, Z. *et al.* Evaluation of natural marine sponge collagen as a scaffold for bone tissue engineering. *Int. J. Biol. Sci.* **7**, 968–977. <https://doi.org/10.7150/ijbs.7.968> (2011).
59. Ruben, R.-R. *et al.* Impact of a porous Si-Ca-P monophasic ceramic on variation of osteogenesis-related gene expression of adult human mesenchymal stem cells. *Appl. Sci.* <https://doi.org/10.3390/app8010046> (2018).
60. Xie, H., Cao, T., Gomes, J. V., Castro Neto, A. H. & Rosa, V. Two and three-dimensional graphene substrates to magnify osteogenic differentiation of periodontal ligament stem cells. *Carbon* **93**, 266–275. <https://doi.org/10.1016/j.carbon.2015.05.071> (2015).
61. Sadek, A. A., Abd-Elkareem, M., Abdelhamid, H. N., Moustafa, S. & Hussein, K. Enhancement of critical-sized bone defect regeneration using UiO-66 nanomaterial in rabbit femurs. *BMC Vet. Res.* **18**, 260. <https://doi.org/10.1186/s12917-022-03347-9> (2022).
62. Cui, X. *et al.* Evaluation of an injectable bioactive borate glass cement to heal bone defects in a rabbit femoral condyle model. *Mater. Sci. Eng. C* **73**, 585–595. <https://doi.org/10.1016/j.msec.2016.12.101> (2017).
63. Strube, P. *et al.* Sex-specific compromised bone healing in female rats might be associated with a decrease in mesenchymal stem cell quantity. *Bone* **45**, 1065–1072. <https://doi.org/10.1016/j.bone.2009.08.005> (2009).
64. Haffner-Luntzer, M., Fischer, V. & Ignatius, A. Differences in fracture healing between female and male C57BL/6J mice. *Front. Physiol.* <https://doi.org/10.3389/fphys.2021.712494> (2021).
65. Pien, D. M., Olmedo, D. G. & Guglielmotti, M. B. Influence of age and gender on peri-implant osteogenesis: Age and gender on peri-implant osteogenesis. *Acta Odontol. Latinoam.* **14**, 9–13 (2001).
66. Vishwakarma, A. *et al.* Engineering immunomodulatory biomaterials to tune the inflammatory response. *Trends Biotechnol.* **34**, 470–482. <https://doi.org/10.1016/j.tibtech.2016.03.009> (2016).
67. Hussein, K. H., Park, K.-M., Kang, K.-S. & Woo, H.-M. Biocompatibility evaluation of tissue-engineered decellularized scaffolds for biomedical application. *Mater. Sci. Eng. C* **67**, 766–778. <https://doi.org/10.1016/j.msec.2016.05.068> (2016).
68. Guihard, P. *et al.* Induction of osteogenesis in mesenchymal stem cells by activated monocytes/macrophages depends on oncostatin M signaling. *Stem Cells* **30**, 762–772. <https://doi.org/10.1002/stem.1040> (2012).
69. Nam, D. *et al.* T-lymphocytes enable osteoblast maturation via IL-17F during the early phase of fracture repair. *PLoS ONE* **7**, e40044. <https://doi.org/10.1371/journal.pone.0040044> (2012).
70. Feehan, J., Nurgali, K., Apostolopoulos, V., Al Saedi, A. & Duque, G. Circulating osteogenic precursor cells: Building bone from blood. *EBioMedicine* **39**, 603–611. <https://doi.org/10.1016/j.ebiom.2018.11.051> (2019).
71. Fukui, T. *et al.* Superior potential of CD34-positive cells compared to total mononuclear cells for healing of nonunion following bone fracture. *Cell Transplant.* **24**, 1379–1393. <https://doi.org/10.3727/096368914X681586> (2015).
72. Kuroda, R. *et al.* Clinical impact of circulating CD34-positive cells on bone regeneration and healing. *Tissue Eng. B.* **20**, 190–199. <https://doi.org/10.1089/ten.teb.2013.0511> (2014).
73. Su, P. *et al.* Mesenchymal stem cell migration during bone formation and bone diseases therapy. *Int. J. Mol. Sci.* <https://doi.org/10.3390/ijms19082343> (2018).
74. Wang, X. *et al.* Role of mesenchymal stem cells in bone regeneration and fracture repair: A review. *Int. Orthop.* **37**, 2491–2498. <https://doi.org/10.1007/s00264-013-2059-2> (2013).
75. Claes, L., Recknagel, S. & Ignatius, A. Fracture healing under healthy and inflammatory conditions. *Nat. Rev. Rheumatol.* **8**, 133–143. <https://doi.org/10.1038/nrrheum.2012.1> (2012).
76. Sandberg, O. H. & Aspenberg, P. Inter-trabecular bone formation: a specific mechanism for healing of cancellous bone. *Acta Orthop.* **87**, 459–465. <https://doi.org/10.1080/17453674.2016.1205172> (2016).
77. Matsumoto, T. *et al.* Therapeutic potential of vasculogenesis and osteogenesis promoted by peripheral blood CD34-positive cells for functional bone healing. *Am. J. Pathol.* **169**, 1440–1457. <https://doi.org/10.2353/ajpath.2006.060064> (2006).
78. Yamachika, E. & Iida, S. Bone regeneration from mesenchymal stem cells (MSCs) and compact bone-derived MSCs as an animal model. *Jpn. Dent. Sci. Rev.* **49**, 35–44. <https://doi.org/10.1016/j.jdsr.2012.11.003> (2013).
79. Houschyar, K. S. *et al.* Wnt pathway in bone repair and regeneration: What do we know so far. *Front. Cell Dev. Biol.* <https://doi.org/10.3389/fcell.2018.00170> (2019).
80. Honma, T. *et al.* Bone formation in rat calvaria ceases within a limited period regardless of completion of defect repair. *Oral Dis.* **14**, 457–464. <https://doi.org/10.1111/j.1601-0825.2007.01401.x> (2008).
81. Itagaki, T., Honma, T., Takahashi, I., Echigo, S. & Sasano, Y. Quantitative analysis and localization of mRNA transcripts of type I collagen, osteocalcin, MMP 2, MMP 8, and MMP 13 during bone healing in a rat calvarial experimental defect model. *Anat. Rec.* **291**, 1038–1046. <https://doi.org/10.1002/ar.20717> (2008).

82. McKee, M. D., Pedraza, C. E. & Kaartinen, M. T. Osteopontin and wound healing in bone. *Cells Tissues Organs* **194**, 313–319. <https://doi.org/10.1159/000324244> (2011).
83. Momtahan, N. *et al.* Using hemolysis as a novel method for assessment of cytotoxicity and blood compatibility of decellularized heart tissues. *ASAIO J.* **62**, 340–348 (2016).
84. Livak, K. J. & Schmittgen, T. D. Analysis of relative gene expression data using real-time quantitative PCR and the 2(-delta delta C(T)) method. *Methods* **25**, 402–408. <https://doi.org/10.1006/meth.2001.1262> (2001).
85. Liu, X. *et al.* GS/DBM/PLA porous composite biomaterial for the treatment of infective femoral condyle defect in rats. *Exp. Ther. Med.* **11**, 2107–2116. <https://doi.org/10.3892/etm.2016.3219> (2016).
86. Kargozar, S. *et al.* Synthesis, physico-chemical and biological characterization of strontium and cobalt substituted bioactive glasses for bone tissue engineering. *J. Non-Cryst. Solids* **449**, 133–140. <https://doi.org/10.1016/j.jnoncrysol.2016.07.025> (2016).
87. Bhutda, S. *et al.* Histochemical staining of collagen and identification of its subtypes by picosirius red dye in mouse reproductive tissues. *Bio-Protoc.* **7**, e2592–e2592 (2017).
88. Wang, W. *et al.* In vivo restoration of full-thickness cartilage defects by poly(lactide-co-glycolide) sponges filled with fibrin gel, bone marrow mesenchymal stem cells and DNA complexes. *Biomaterials* **31**, 5953–5965. <https://doi.org/10.1016/j.biomaterials.2010.04.029> (2010).
89. Liu, J. *et al.* Injectable biocomposites for bone healing in rabbit femoral condyle defects. *PLoS ONE* **8**, e75668. <https://doi.org/10.1371/journal.pone.0075668> (2013).
90. Abd-Elkareem, M. Cell-specific immuno-localization of progesterone receptor alpha in the rabbit ovary during pregnancy and after parturition. *Anim. Reprod. Sci.* **180**, 100–120. <https://doi.org/10.1016/j.anireprosci.2017.03.007> (2017).

Acknowledgements

The authors would like to thank Prof. Tarek Elgammal, Prof. Madiha Darwish, and Prof. Mohamed Semieka for their support. Dr. Abdelhamid thanks Science, Technology & Innovation Funding Authority (STDF) for Grant Project No. 42886.

Author contributions

A.A.S.: Conceptualization, Methodology, Investigation, Data curation, Writing—original draft, Writing—review & editing, and Formal analysis. M.A.: Methodology, Investigation, Data curation, and Writing—original draft, Writing—review & editing, Formal analysis. H.N.A.: Methodology, Investigation, Data curation, and Writing—original draft, and Writing—review & editing. S.M.: Formal analysis, Validation and Supervision. K.H.: Conceptualization, Methodology, Investigation, Data curation, and Writing—original draft, Writing—review & editing, Formal analysis, Validation, and Supervision. All authors reviewed the manuscript and approved the final version for publication.

Funding

Open access funding provided by The Science, Technology & Innovation Funding Authority (STDF) in cooperation with The Egyptian Knowledge Bank (EKB).

Competing interests

The authors declare no competing interests.

Additional information

Supplementary Information The online version contains supplementary material available at <https://doi.org/10.1038/s41598-023-32487-7>.

Correspondence and requests for materials should be addressed to K.H.

Reprints and permissions information is available at www.nature.com/reprints.

Publisher's note Springer Nature remains neutral with regard to jurisdictional claims in published maps and institutional affiliations.



Open Access This article is licensed under a Creative Commons Attribution 4.0 International License, which permits use, sharing, adaptation, distribution and reproduction in any medium or format, as long as you give appropriate credit to the original author(s) and the source, provide a link to the Creative Commons licence, and indicate if changes were made. The images or other third party material in this article are included in the article's Creative Commons licence, unless indicated otherwise in a credit line to the material. If material is not included in the article's Creative Commons licence and your intended use is not permitted by statutory regulation or exceeds the permitted use, you will need to obtain permission directly from the copyright holder. To view a copy of this licence, visit <http://creativecommons.org/licenses/by/4.0/>.

© The Author(s) 2023